



Rare earth La single atoms supported MoO_{3-x} for efficient photocatalytic nitrogen fixation

Xiufan Liu^a, Yani Luo^a, Cancan Ling^a, Yanbiao Shi^b, Guangming Zhan^a, Hao Li^a, Huayu Gu^a, Kai Wei^a, Furong Guo^a, Zhihui Ai^{a,*}, Lizhi Zhang^{a,*}

^a Key Laboratory of Pesticide & Chemical Biology of Ministry of Education, Institute of Environmental Chemistry, Central China Normal University, Wuhan 430079, China

^b School of Environmental Science and Engineering, Shanghai Jiao Tong University, Shanghai 200240, China

ARTICLE INFO

Keywords:

Single-atom catalyst
Rare-earth La
Photocatalytic nitrogen fixation
Coordination
MoO_{3-x}

ABSTRACT

Herein, we demonstrate that the rare-earth La single catalyst with multi-shell characteristic is an excellent choice for this purpose. By merit of its unsaturated orbitals of La, the single La atom strongly bonds with the two-coordinated lattice oxygen on the oxygen-deficient MoO_{3-x} to form O_{2c}-La-O_{2c} coordination. This robust metal-support interaction frees single atoms from detachment or aggregation, and prevents catalyst from deactivation. Meanwhile, the occupied 5d orbitals of La back-donate electrons to the 2π* molecular orbitals of adsorbed N₂ that substantially activate the inert N≡N bond towards successive hydrogenation. And single La atom could optimize the electron property of the MoO_{3-x} support to promote photocatalytic nitrogen fixation. Without any sacrificial agents, this single atom La catalyst with a well-designed coordination structure delivers an impressive NH₃ production rate of 209.0 μmol h⁻¹ g⁻¹ under visible light, outperforming most reported single atom photocatalysts.

1. Introduction

Ammonia (NH₃) is a potential energy storage medium and an important primary chemical in various fields [1–3]. The industrial Haber-Bosch process requires high energy consumption (300–400 °C) and high pressure (15–250 atm), resulting in high emissions of greenhouse gases [4]. To address this issue, a variety of alternative method have been developed for N₂ fixation, including enzymatic, photo- and electrocatalysis, as well as chemical looping. Among them, the photocatalytic reduction of N₂ in the aqueous phase, which is characterized by harnessing solar light as the energy source, semiconductor as the catalyst, and water as the electron/proton donor, was deemed extremely promising. Although many traditional photocatalysts (such as TiO₂, black phosphorous, and C₃N₄ [5–7]) have been investigated for photocatalytic nitrogen fixation, they usually display poor reactivity. This is because N₂ with a strong N≡N triple bond usually exhibits faint interaction with photocatalysts surface. Thus, most of the electrons suffer from vigorous annihilation with photoholes, rather than being captured by adsorbed N₂ [5]. Thus, developing novel efficient photocatalyst for

efficient N₂ fixation is urgently needed.

Owing to single-atom catalysts (SACs) can obtain atomically dispersed atoms on supports offering numerous well-defined active sites for maximumly promoting the catalytic activity [8], this remarkable advantage made SACs superior in photocatalytic nitrogen fixation [9]. Various SACs showed excellent photocatalytic performance due to well-designed coordination structure of metal atoms coordinated anions (C, O, N, etc) [10–12]. Xie et al. demonstrated that the Cu SACs in C₃N₄ can provide a unsaturated coordination structure of Cu-N and promote the isolation of photoexcited electrons to accelerate ammonia photosynthesis [13]. Xiong et al. reported a new kind of W SACs with unique O, N coordination for elevating NRR activity, illustrating the structure-properties relationship based on the control of the coordination of metal single atoms [14]. Apparently, the single atoms had a marked impact on electron transfer dynamics, vital to activation of adsorbed molecules and catalytic activity, especially for the nitrogen reduction reaction [15,16]. Among various SACs, rare-earth SACs with unique electronic, optical, and magnetic properties are strategic resources with broad applications in electronic devices and industrial

* Corresponding authors at: Key Laboratory of Pesticide & Chemical Biology of Ministry of Education, Institute of Environmental Chemistry, Central China Normal University, Wuhan 430079, China.

E-mail addresses: jennifer.ai@mail.ccnu.edu.cn (Z. Ai), zhanglz@mail.ccnu.edu.cn (L. Zhang).

<https://doi.org/10.1016/j.apcatb.2021.120766>

Received 16 July 2021; Received in revised form 25 September 2021; Accepted 26 September 2021

Available online 8 October 2021

0926-3373/© 2021 Elsevier B.V. All rights reserved.

manufacturing. Notably, a large proportion of rare-earth elements have been used for heterogeneous catalysis by merit of their multi-shell electron configuration. Due to their partly filled orbitals, rare-earth elements usually display Lewis acidity that usually strongly coordinate with anions groups with high Lewis basicity, that is, the rare earth SACs is highly promising to strength coordination with the lattice anions of the support or the strong activation with anions of adsorbed-molecules [17]. Moreover, the unsaturated 5d orbitals of rare-earth elements supply energetic electrons for N_2 adsorption and activation. Activation of the $N\equiv N$ triple bond can serve as the crucial impetus for successive N_2 fixation. To this end, we reckon that rare-earth SACs with multi-shell orbitals may be good candidates to engineer the active site for efficient photocatalytic N_2 fixation.

Metal oxides have been extensively exploited as support due to their well-defined surface structure and a high degree of anisotropy [18]. Notably, the defective molybdenum oxide (MoO_{3-x}) gives special and well-defined lattice oxygen to anchor rare earth SACs [19,20]. The surface of MoO_{3-x} consists of six-fold and five-fold coordinated Mo-O configurations, where the specific oxygen vacancy of five-fold coordinated Mo-O expose rich lattice oxygen anions. Due to the rich lattice anions, the unoccupied orbitals of rare earth single atoms can form strong coordination with the oxygen anions instead of encountering the electrostatic interaction of the positively charged lattice metal atoms [21]. To date, there have been no reports to investigate the rare earth La single atom for photocatalytic nitrogen fixation and get insights into the related reaction mechanism. Thus, it is a need to identify the coordination of single La atom in the MoO_{3-x} and investigate the application of single La atom in the photocatalytic nitrogen fixation.

In this work, we successfully anchor single La atom in MoO_{3-x} and report a kind of specific coordination of lattice oxygen coordinated single La atom. The MoO_{3-x} abundant oxygen vacancies are purposely selected as the anchored site due to the 2-coordinated lattice oxygen (O_{2c}) to form atomically dispersed La coordination. The coordination of single La atom can be confirmed by HAADF-STEM and XAFS analysis, and the single La atoms significantly optimize the ability of nitrogen activation and the behavior of photo-excited electrons for the support. Without any sacrificial agents, this single atom La catalyst with a well-designed coordination structure delivers an impressive NH_3 production rate of $209.0 \mu mol h^{-1} g^{-1}$ under visible light and long-term stability, outperforming most reported single atom photocatalysts. Mechanistic insights into the N_2 activation scheme and detailed reaction mechanisms were elaborated based on the theoretical and experimental.

2. Experimental

2.1. Chemicals and materials

Ethanol ($\geq 99.7\%$), molybdenum powder, hydrogen peroxide (30 wt %), and ethylene glycol ($\geq 99.5\%$), were all purchased from Sino-pharm Chemical Reagent Co., Ltd. China. Lanthanum nitrate was purchased from Aladdin Chemical Reagent Co., Ltd. All chemicals were used without any further purification. Deionized water was used throughout the experiments.

2.2. Samples preparation

The MoO_{3-x} was synthesized by the solvothermal method. In brief, 24 mL of ethanol and 50 mL capacity of polytetrafluoroethylene liner were mixed, then molybdenum powder (0.1919 g) was added to obtain suspension. Next, 3 mL of H_2O_2 was added into the suspension and vigorously stirring for 30 min. The suspension was transferred into the reactor heated at $160^\circ C$ for reaction 12 h. After cooling down naturally, the obtained dark blue precipitates were rinsed with anhydrous ethanol and deionized water followed by centrifugation and dried at $60^\circ C$ for 12 h in a vacuum.

The La/ MoO_{3-x} was prepared by the photo-deposition method: 1

mmol MoO_{3-x} (0.1439 g), 25 mL of glycol, and 25 mL of deionized water were mixed in a 20 mL beaker, followed by stirring 30 min to obtain the suspension B. Next, 0.0040 g lanthanum nitrate (1.0 mol% of MoO_{3-x}) was dissolved by 2.5 mL of deionized water, and ultrasound 30 min to obtain solution C. Then suspension B and C was mixed and stirred for 20 min in dark. Finally, the resulting solution was treated by light irradiation with a Xenon lamp for 5 min. The products were rinsed with anhydrous ethanol and deionized water several times, followed by centrifugation, and finally dried at $60^\circ C$ for 12 h. The obtained product was labeled as La/ MoO_{3-x} .

2.3. Characterization

XRD patterns were measured by Bruker DAVINCI D8 ADVANCE diffractometer with Cu K α radiation ($\lambda = 1.5418$ nm), the morphologies and elements composition were analyzed using scanning electron microscopy (SEM, JSM-7610 F) and transmission electron microscopy (TEM, JEM-2010 F). A JEOL ARM-200 F TEM/STEM with a spherical aberration corrector working at 300 kV recorded the high-angle annular dark-field scanning transmission electron microscopy (HAADF-STEM) and energy-dispersive spectroscopy (EDS) images. Electron paramagnetic resonance (EPR) spectra were obtained by JES-FA200 at room temperature.

The absorption spectra were performed using diffuse reflection spectra at a range 200 ~ 2500 nm (DRS, Agilent Cary-5000). The surface electronic states were analyzed via X-ray photoelectron spectroscopy (XPS, Thermo ESCALAB 250Xi) with all binding energies referencing to the C 1 s peak at 284.5 eV. La L_{3-2} -edge X-ray absorption fine structure (XAFS) measurements were performed on the 1W1B beamline of Beijing Synchrotron Radiation Facility (BSRF). The Photocurrent and Mott-Schottky plots measurements experiments were conducted determined using the electrochemical workstation (CHI Instruments CHI660D). The electrochemical impedance spectroscopy (EIS) measurements were conducted over a frequency range $0.01-10^5$ Hz. The photoluminescence spectra decay curves were obtained by using fluorescence spectrophotometer at room temperature (FL1008M018). The in situ DRFTIRS spectra were recorded by in situ FT-IR spectrometer (Thermo iS50 FT-IR) with MCT detector and the specific designed reaction cell. The loading amount of La was measured by inductively coupled plasma optical emission spectroscopy (Agilent ICPOES730).

2.4. Photocatalytic nitrogen fixation

Photocatalytic nitrogen fixation was conducted at room temperature using a 300 W Xe lamp (Beijing Perfectlight, PLS-SXE 300D, 200–800 nm, light intensity $1.73 W/cm^2$) with a 420 nm cutoff filter. First, 20 mg of the catalyst was dispersed in 150 mL of deionized water in a specific lockable quartz reactor. Next, the mixtures were continuously stirred in dark and bubbled with N_2 gas (99.999%, 60 mL/min) for 60 min, before being exposed to visible light irradiation. During the reaction, 3 mL of the reaction solution was collected every 20 min. The collected solution was detected by ion chromatography (Thermo DIONEX ICS-900) to determine the concentration of NH_3 (as NH_4^+) and O_2 produced.

2.5. DFT calculation

All calculations were performed using the first-principles density of functional theory (DFT) with the exchange-correlation energy function of GGA-PBE [22,23]. The calculations were conducted using the CASTEP package in which the ultra-soft pseudopotentials were employed for all atoms with the accuracy set as *fine*. The energy cutoff of 400 eV and a k-point set of $2 \times 2 \times 1$ was chosen for the calculations, with an SCF tolerance of 1.0×10^{-5} eV/atom, an energy tolerance of 1.0×10^{-5} eV/atom, a maximum force of 0.03 eV/Å, and a maximum displacement of 1.0×10^{-3} Å. In addition, Plane-wave density functional theory (DFT) +U ($U_{\text{eff}} = U - J = 6.3$ eV) approach was applied to study correlation

between support and adsorbed molecule in this work, which can be with considerable improvement with respect to GGA results.

The MoO_{3-x} supercell model contains 71 atoms (including 18 Mo and 53 O atoms). The $\text{La}/\text{MoO}_{3-x}$ supercell was obtained by adding the La atom to the oxygen vacancy site. The vacuum space along the z-direction was beyond 15 Å. The bottom atomic layers were fixed, and the rest of the atomic layers and adsorbed molecules were relaxed during all calculations.

The free energy of the reaction intermediates was obtained by $\Delta G = \Delta E_{\text{ads}} + \Delta \text{ZPE} - T\Delta S$, where ΔE_{ads} is the adsorption energy, ZPE is the zero-point energy and S is the entropy at 298 K.

The formation energy of sing La atom or oxygen vacancy was defined as an equation: $E_f = E(\text{final}) + E(\text{La})$ [or $-E(\text{O})$] $- E(\text{initial})$, Where E_f is the formation energy, $E(\text{initial})$ and $E(\text{final})$ means the total energies without and with single La atom or oxygen vacancy, $E(\text{La})$ or $E(\text{O})$ means the total energy of the single La atom or oxygen atom.

3. Results and discussion

3.1. The coordination and properties of single La atom

The DFT calculations can be used to predict the position of oxygen vacancy of MoO_{3-x} and single La atom. As shown in Fig. S1, we calculate formation energy of three different oxygen vacancy, and found that the formation energy of terminal oxygen vacancy only needs 10.87 eV, much lower than those of 2-coordinated O site (Mo-O-Mo) and 3-coordinated O sites (O_{2c} and O_{3c} vacancy site, 11.03 eV and 12.72 eV respectively), suggesting that the terminal oxygen vacancy is the most feasible in thermodynamics. As illustrated in Fig. 1a and b, the surface of MoO_{3-x} is mainly terminated by two- and three-coordinated lattice oxygen (O_{2c} and O_{3c} respectively) and five-coordinated unsaturated Mo (Mo_{5c} , terminal oxygen vacancy) except one-coordinated oxygen (terminal oxygen), in which terminal oxygen vacancy sites are hypothesized to constitute single La atom anchoring site. To further identify the position of single La atom, as depicted in Fig. S2, we calculated the

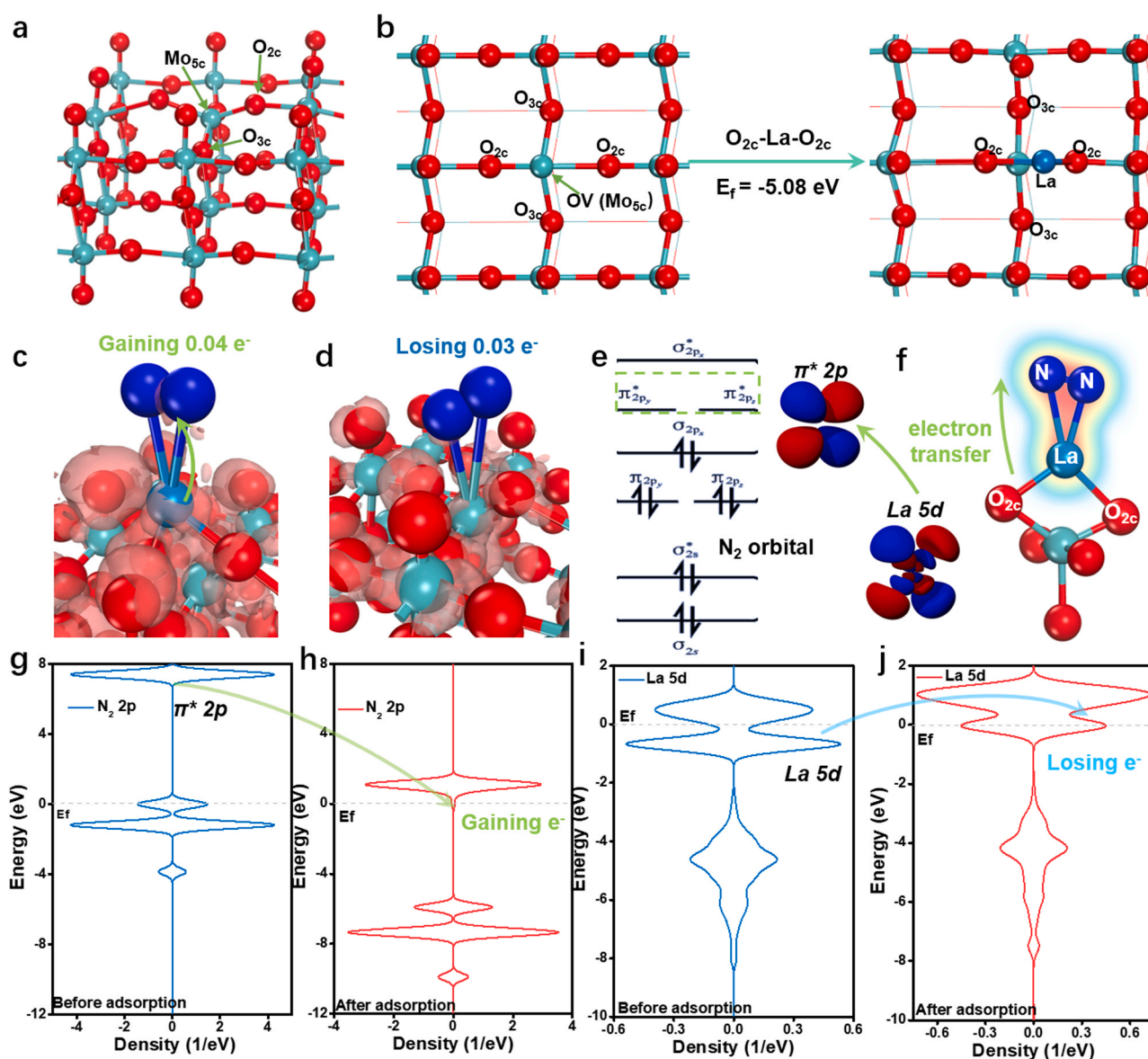


Fig. 1. (a) Optimized structure of the MoO_{3-x} (side view). (b) Top view of the MoO_{3-x} structure and the optimized configuration of La atom at terminal oxygen vacancy site. (c) Electron density difference between nitrogen and $\text{La}/\text{MoO}_{3-x}$ and (d) MoO_{3-x} , the red iso-surface corresponding to charge accumulation. (e) Diagrams of the nitrogen $\pi^* 2p$ orbital. (f) Diagram of the electron transfer from La to the adsorbed nitrogen. N_2 2p orbital DOS (g) before adsorption and (h) after adsorption on $\text{La}/\text{MoO}_{3-x}$. The La 5d orbital DOS of (i) the single La atom before N_2 adsorption and (j) after N_2 adsorption.

formation energy of single La atom localized at oxygen vacancy site. The formation energy of single La atom localized at terminal oxygen vacancy site, O_{2c} vacancy site and O_{3c} vacancy site is -5.08 eV, -2.82 eV and -0.78 eV respectively, confirming that terminal oxygen vacancy is most suitable for anchoring single La atom. The position of single La atom is depicted in Fig. 1b and Fig. S3. Thus, above DFT calculations confirm that single La atom theoretically tend to occupy terminal oxygen vacancy and coordinate with O_{2c} to form O_{2c} -La- O_{2c} coordination.

Subsequently, we conducted first-principles calculations to simulate the nitrogen adsorption and activation on O_{2c} -La- O_{2c} site to clarify the role of La atom. The analysis of electron density difference clearly shows that nitrogen is adsorbed on La in a side-on configuration, with a considerable number of electrons accumulating in the $N\equiv N$ bond for La/MoO_{3-x} (Fig. 1c), different from the negligible electron accumulation of side-on nitrogen adsorbed on MoO_{3-x} (Fig. 1d). The corresponding Mulliken charge analysis results also show that the nitrogen adsorbed on La/MoO_{3-x} can gain 0.03 e; by contrast, the nitrogen adsorbed on support loses 0.04 e (Table S3). Theoretically, the d orbital of metal couples with the N 2p orbital, facilitating electron filling into the $\pi^* 2p$ orbital of nitrogen [24]. In this sense, the electrons would transfer from the 5d orbital of the single La atom into the $\pi^* 2p$ orbital of the adsorbed nitrogen (Fig. 1e-f). We further implement the scenario by

the density of states (DOS) analysis. Interestingly, the DOS of unoccupied $\pi^* 2p$ orbital of N₂ moves to a deeper energy level, partially below the Fermi level (E_f) while that of occupied 5d orbital of La shifts to the higher energy level above E_f (losing electrons) after side-on nitrogen adsorption, meaning that electrons were transferred from 5d orbital of La into the $\pi^* 2p$ orbital of N₂ (as depicted in Fig. 1g and h). These DFT results reveal that single La atom significantly optimized local electron properties, and the nitrogen molecule adsorbed on O_{2c} -La- O_{2c} site can be effectively activated by the accumulated electrons occupied in the $\pi^* 2p$ orbital, which is beneficial to the $N\equiv N$ bond cleavage and further hydrogenation.

MoO_{3-x} and La/MoO_{3-x} were as-prepared by a solvothermal method. XRD patterns reveal that both MoO_{3-x} and La/MoO_{3-x} are consistently assigned to the orthorhombic molybdate phase (JCPDS 70-0912) (Fig. 2a). The stronger intensity of La/MoO_{3-x} indicates that the improved crystallinity of MoO_{3-x} derived from the embedded element La. This result could also be demonstrated by the room-temperature EPR (Fig. 2b). A strong signal of catalysts at $g = 2.003$ confirm the nature beings of oxygen vacancy [25]. Interestingly, La/MoO_{3-x} shows a weaker electron paramagnetic resonance signal, indicating that the number of unpaired electrons is distinctly reduced and that the unpaired electrons localized in the oxygen vacancy could

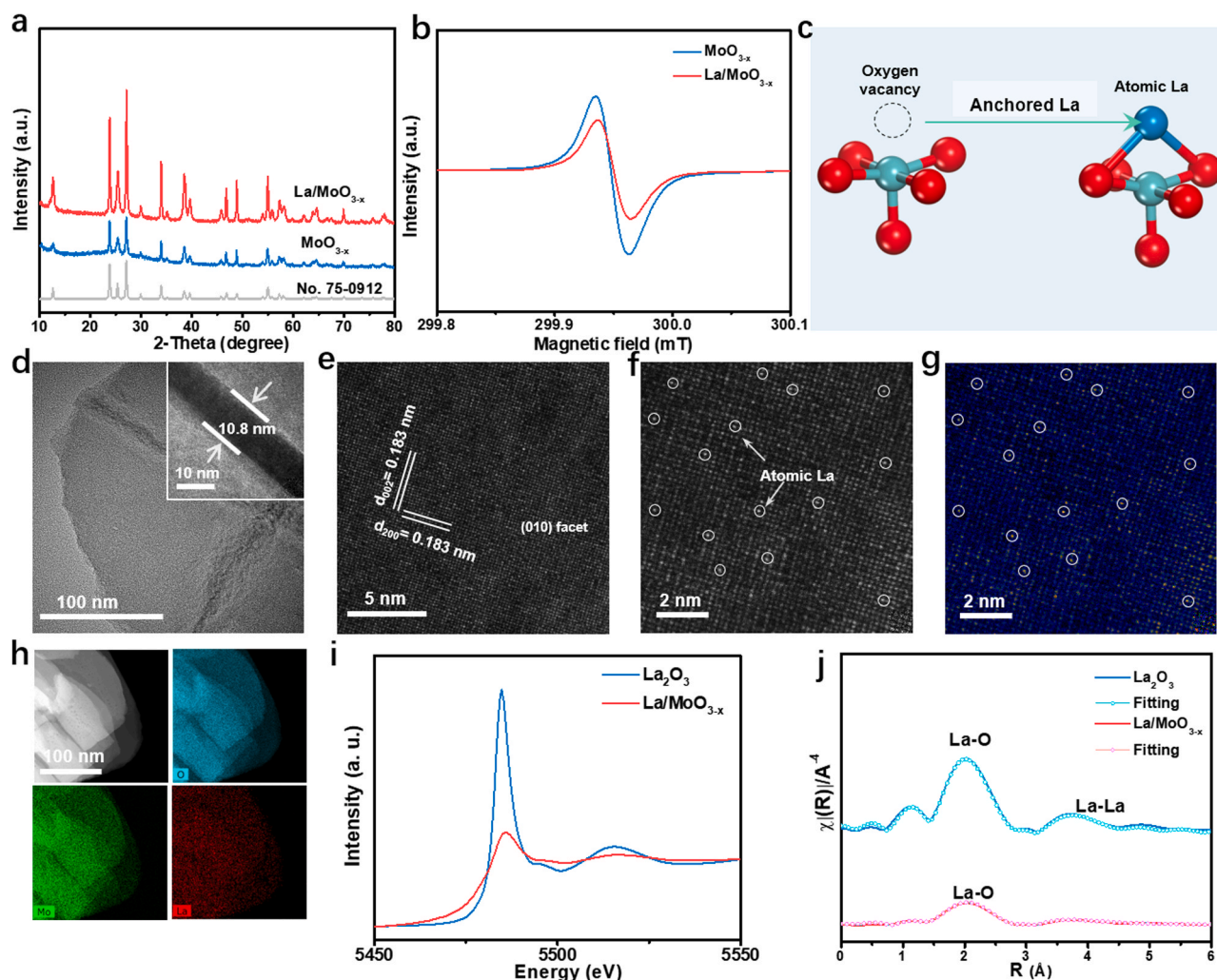


Fig. 2. (a) XRD patterns of MoO_{3-x} and La/MoO_{3-x}. (b) EPR signals of La/MoO_{3-x} and MoO_{3-x}. (c) Schematic illustration of a single La atom anchored on oxygen vacancy site. (d) TEM images of La/MoO_{3-x}. (e) The HAADF-STEM image of La/MoO_{3-x} shows the exposed facet structure. (f) Magnified HAADF-STEM image of (e). (g) Rainbow-colored converted HAADF-STEM image of (f). The atomically dispersed La atoms are marked in (f) and (g) by white circles. (h) HAADF-STEM EDS analysis shows the element distribution of Mo, La, and O. (i) XANES curves of the La₂O₃ foil and La/MoO_{3-x}. (j) k^3 -weighted Fourier-transformed EXAFS fitting curves in R-space of La₂O₃ foil and La/MoO_{3-x}.

couple with the electrons of the La 5d orbital; that is, the La atom occupy oxygen vacancy site (as depicted in Fig. 2c). And the EPR experiments also quantify the amount of oxygen vacancy in La/MoO_{3-x} and MoO_{3-x}. As shown in Fig. S4, the number of unpaired electrons of La/MoO_{3-x} is 6.87×10^{12} , which is less than that of MoO_{3-x} (10.96×10^{12}). Additionally, the XPS spectrum of La/MoO_{3-x} shows peaks at 231.4 eV and 234.5 eV corresponding to the Mo⁵⁺ 3d_{3/2} orbital and Mo⁵⁺ 3d_{5/2} orbital [20], respectively; the peaks of 232.9 eV and 236.1 eV correspond to the Mo⁶⁺ 3d_{5/2} orbital and Mo⁶⁺ 3d_{3/2} orbital [26], respectively (Fig. S5). Generally, Mo⁵⁺ adopts a five-coordinated Mo_{5c}, where the five-coordinate Mo_{5c} structure represents an oxygen vacancy site [27]. Besides, the XPS spectrum of the La 3d orbital (Fig. S6) shows that La element is in the +3 valence oxidation state rather than metal cluster state [28], further confirming the La-O bond between La atom and oxygen atoms. And the practical loading amount of La can be identified by ICP-OES analysis, the practical loading amount of La element is 0.3048 wt% of the sample (namely 0.5988 mol%).

We further verified the surface structure of La/MoO_{3-x} by SEM, transmission electron microscopy (TEM) and aberration-corrected high-angle annular dark-field scanning transmission electron microscopy (HAADF-STEM). The SEM images of all samples indicate their nanosheet nature (Fig. S7 a and b), and TEM images show a nanosheet with a thickness of about 10.8 nm (Fig. 2d). We deduce the exposed (010) facet of the nanosheet according to the well-resolved lattice fringes of HAADF-STEM based on the Weiss zone law (Fig. 2e). As illustrated in the DFT analysis (Fig. 1b), Mo_{5c} atom bonds with the neighboring two-coordinated O (O_{2c}) and three-coordinated O (O_{3c}), where O_{2c} is an unsaturated coordination state that preferably couples with single La atoms, forming an O_{2c}-La-O_{2c} configuration. Thus, the anchored single La atom on MoO_{3-x} could be further demonstrated experimentally. According to the HAADF-STEM and its rainbow-colored images, the atomically dispersed La atoms (white circles) exhibit much stronger contrast than Mo atoms (Fig. 2f-g). Also, the STEM-EDS elemental maps (Fig. 2e) clearly show the excellent dispersion of atomic La on the support (Fig. 2 h).

The exact coordination environment of La/MoO_{3-x} is further studied by X-ray absorption fine structure (XAFS). Apparently, the XANES spectra of La/MoO_{3-x} demonstrate the decreased white line strength compared to La₂O₃. The white line intensity is linearly related to the coordination number. In Fig. 2i, the white line intensity of the La is much lower than that of La₂O₃, indicating that the unsaturated-state coordination environment of La. The k³-weight EXAFS spectra at La L₃ edge are obtained to further identify the coordination environment of the La atom in R space (Fig. 2e), and the Table S1 summarizes all fitting results. The fitting curves are well matched to the experimental data in R space, proving the reliability of fitting results. The R-space fitting for La₂O₃ sample displays that La-O shell is at 2.50 Å, assigned to the six-oxygen atom coordinated La atom. And the La-O shell coordination at 2.43 Å can be also found in La/MoO_{3-x}, where the coordination number of La is 1.9 close to two oxygen coordination structure. Besides, compared with the La-La interaction at around 4 Å in La₂O₃, this La-La bond cannot be distinctly observed in La/MoO_{3-x}. Consistent with XPS and STEM analysis, no La cluster or any other La⁰ species existed on the support. Based on previous DFT and morphology analysis, these results finally confirm that isolated La atoms dispersed on MoO_{3-x} support atomically, which are anchored with two O_{2c} atoms to form O_{2c}-La-O_{2c} coordination.

3.2. Single La atom optimized performance and intrinsic properties

To investigate the photocatalytic nitrogen fixation performance, all samples are put into the reactor (Fig. S8) with nitrogen saturated water and illuminate under visible light with 300 W Xenon lamp ($\lambda > 420$ nm), and the performance of the samples are measured by using ion chromatography to quantify NH₃ evolved (Fig. S14). The ammonia generation rate for La/MoO_{3-x} (Fig. S15) is 209.0 $\mu\text{mol h}^{-1} \text{g}^{-1}$

(41.8 $\mu\text{mol L}^{-1}$, namely 209.0 $\mu\text{mol h}^{-1} \text{g}^{-1}$), and nearly 10 times that of the support (4.2 $\mu\text{mol L}^{-1}$, equal to 21.0 $\mu\text{mol h}^{-1} \text{g}^{-1}$). It has been found that La/MoO_{3-x} possess better ammonia production rate than most of the reported values, especially best performance in the works of SACs in recent years (Table S3). Considering the influence of oxygen vacancy on performance, we conduct comparative experiments among La/MoO_{3-x}, MoO_{3-x} and MoO₃ (Fig. S9). The results show MoO₃ exhibits ammonia product of 1.4 $\mu\text{mol/L}$ much lower than those of La/MoO_{3-x} (41.8 $\mu\text{mol/L}$) and MoO_{3-x} (4.8 $\mu\text{mol/L}$), suggesting that oxygen vacancy only slightly enhance performance, the main descriptor of greatly improved photocatalytic performance for La/MoO_{3-x} is single La atom. To further verify the N source of produced ammonia, isotope labeling photocatalytic nitrogen reduction can be performed by using ¹⁵N₂ as the reactant, and the products is tested by ¹H NMR spectroscopy. As shown in Fig. S10, only ¹⁵NH₄⁺ signals can be observed when ¹⁵N₂ is bubbled into the reactor, while the ¹⁴NH₄⁺ signals can be detected using ¹⁴N₂ as N source. And, Fig. 3a shows that negligible photocatalytic performance with bubbling Ar gas into the reactor. These results confirm that ammonia product evolves from N₂ instead of other contamination. In addition, for ammonia evolution from N₂ and H₂O, O₂ is expected to form as a byproduct ($\text{N}_2 + 3 \text{H}_2\text{O} \rightleftharpoons 2\text{NH}_3 + 1.5 \text{O}_2$). The production of O₂ (29.4 $\mu\text{mol/L}$) and NH₃ (41.8 $\mu\text{mol/L}$) evolved during the experiment are very close to theoretical ratio of 3:4 (Fig. S11), suggesting that water is the main proton source during the reaction. The cycling experiments also show a relatively stable ammonia production rate during 5 cycles (Fig. 3b), and the XRD patterns also demonstrate that characteristic peaks' positions of La/MoO_{3-x} are unchanged after use (Fig. S12), revealing the stable performance and structural stability of La/MoO_{3-x} catalysts.

Interestingly, the excellent activity of La/MoO_{3-x} does not originate from the well-enhanced light adsorption capacity, since the UV-vis diffuse reflection spectra exhibit hardly discernible absorbance differences between MoO_{3-x} and La/MoO_{3-x} at visible light range 420–800 nm. Thus, the activity difference comes from the optimized intrinsic electron properties. According to the Tauc-plot in Fig. S13a, the bandgap of MoO_{3-x} and La/MoO_{3-x} is 2.48 eV. Results from the VB-XPS measurements can be used to determine the valence band [29], showing the same valence band (VB) position (3.2 eV) of the catalysts (Fig. S13b), indicating that the La single atom cannot influence the original bandgap structure. However, we can see that distinguished defect bands (DBs) exist in different catalysts according to the VB-XPS analysis (Fig. S13c and S13d), which are estimated to be 0.87 eV for MoO_{3-x} and 1.12 eV for La/MoO_{3-x}. These experimental results are consistent with the DFT calculations (Fig. 3g-h) in trends, and the electron densities of states indicate that the defect band level decreases from 1.71 eV (MoO_{3-x}) to 1.36 eV (La/MoO_{3-x}). Generally, the defect band level closed to the center of bandgap favors photogenerated electrons leaping from the VB to the conduction band and finally trapped at defect band [30]. Thus, the anchored single La atom can be beneficial to the transfer of photoexcited electrons into adsorbed nitrogen.

To experimentally examine the dynamics of photoexcited electrons, electrochemical impedance, photoluminescence (PL), and photocurrent measurements were carried out (Fig. 3d-f). La/MoO_{3-x} exhibits the lowest interfacial resistance (1049 Ω) among the catalysts (Fig. 3d), which corresponds to the lowest charge-transfer resistance [31]. Consistent results were obtained in the photocurrent and PL experiments. The La/MoO_{3-x} samples also exhibit the highest photocurrent, with an instantaneous photocurrent response of approximately 35 mA, in comparison to 15 mA for another sample. These data correlates well with the lowest PL intensity observed in Fig. 3f. Note that a higher photogenerated current and lower PL intensity suggest a more efficient separation of photogenerated electron-hole pairs [32]. Thus, the La/MoO_{3-x} sample displays the optimized charge separation efficiency, a unique intrinsic property that positively influence the activity of the composite catalyst.

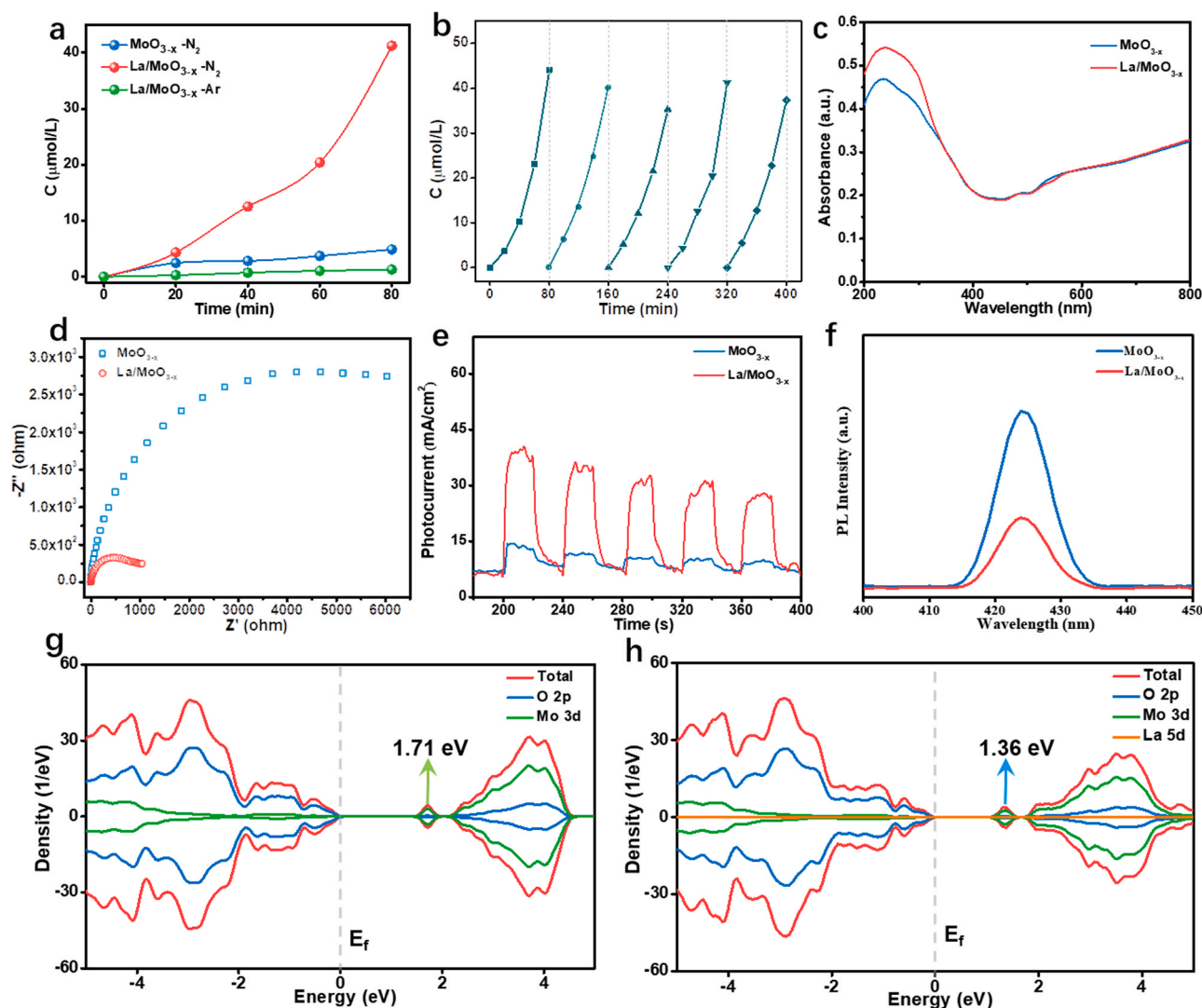


Fig. 3. (a) Photocatalytic activity of ammonia synthesis. (b) Cycling activity of La/MoO_{3-x} . (c) UV-vis diffuse reflection spectra, wavelength range from 200 nm to 2500 nm. (d) Impedance curves. (e) Photocurrent response curves. (f) Steady-state fluorescence spectra, excitation wavelength at 360 nm. (g) Electronic densities of states for MoO_{3-x} and (h) La/MoO_{3-x} .

3.3. The reaction mechanism of photocatalytic nitrogen fixation

To elucidate the mechanism of nitrogen fixation and verify the aforementioned theoretical calculations, we conduct in situ FT-IR experiments (the specific reaction cell was shown in Fig. 4a and Fig. S16). Fig. 4b shows the in situ infrared spectra of N_2 adsorption and reaction on La/MoO_{3-x} , where a series of vibrational bands can be identified: the peak at 1625 cm^{-1} to adsorbed N_2 , peak at 3843 cm^{-1} and peak at 3729 cm^{-1} to H_2O . Upon visible light irradiation, we can see a significant change in the IR signals in addition to the enhanced peaks of adsorbed N_2 , where the new product peaks at 1519 cm^{-1} and 1690 cm^{-1} are assigned to NH_4^+ , the peak at 3251 cm^{-1} is attributed to adsorbed NH_3 , and the peak at 1129 cm^{-1} is attributed to hydrazine. Notably, hydrazine is a key intermediate product, indicating that N_2 is adsorbed by a side-on bridging configuration, and the subsequent nitrogen fixation follows the symmetric alternative pathway [33]. Specifically, all peaks are distinctly enhanced during the reaction, suggesting enhanced adsorption of nitrogen and conversion to NH_3 [34].

In contrast, Fig. 4c shows the in situ infrared spectra of N_2 adsorption and reaction on MoO_{3-x} , where the peaks of nitrogen adsorption and the corresponding conversion product do not exist, and only adsorbed H_2O is observed, indicating that the individual oxygen vacancy is not

sufficient to adsorb and activate N_2 . These results suggest that the single La atom is responsible for the excellent nitrogen fixation performance as a result of the effective activation of N_2 by the La 5d electrons, which is agreed well with previous electronic dynamics calculations.

Subsequently, DFT calculations are performed to obtain further insight into the reaction mechanism at the atomic scale. The (010) exposed facet is applied as the surface model. From the reaction energy process of N_2 fixation of $^*\text{N}_2 \rightarrow ^*\text{NNH} \rightarrow ^*\text{NHNH} \rightarrow ^*\text{NHNH}_2 \rightarrow ^*\text{NH}_2\text{NH}_2 \rightarrow ^*\text{NH}_2 + ^*\text{NH}_3 \rightarrow ^*\text{NH}_2 \rightarrow ^*\text{NH}_3 \rightarrow \text{NH}_3$ (Fig. 4d), we can see that the N_2 molecules prefer to adsorb on the $\text{O}_{2c}\text{-La-O}_{2c}$ site of La/MoO_{3-x} in a side-on configuration with a free energy of -1.08 eV , and Mulliken charge analysis indicates that 0.04 e is transferred to the $\text{N}_2\pi^*2p$ antibonding orbital, suggesting that N_2 is spontaneously adsorbed and effectively activated. Nevertheless, the N_2 adsorption free energy (0.43 eV) and charge transfer (loss 0.03 e of N_2) of MoO_{3-x} indicate that the initial N_2 is difficult to activate at the oxygen vacancy site, which means that the subsequent process is more likely infeasible without the single La atom.

Furthermore, the $^*\text{NNH} \rightarrow ^*\text{NHNH}$ process of the $\text{O}_{2c}\text{-La-O}_{2c}$ site is a decline curve with decreased energy of -1.38 eV , which is much lower than that (0.52 eV) of MoO_{3-x} . Then, the process of $^*\text{NHNH}$ to $^*\text{NHNH}_2$ is also a falling energy pathway with spontaneous hydrogenation. Note

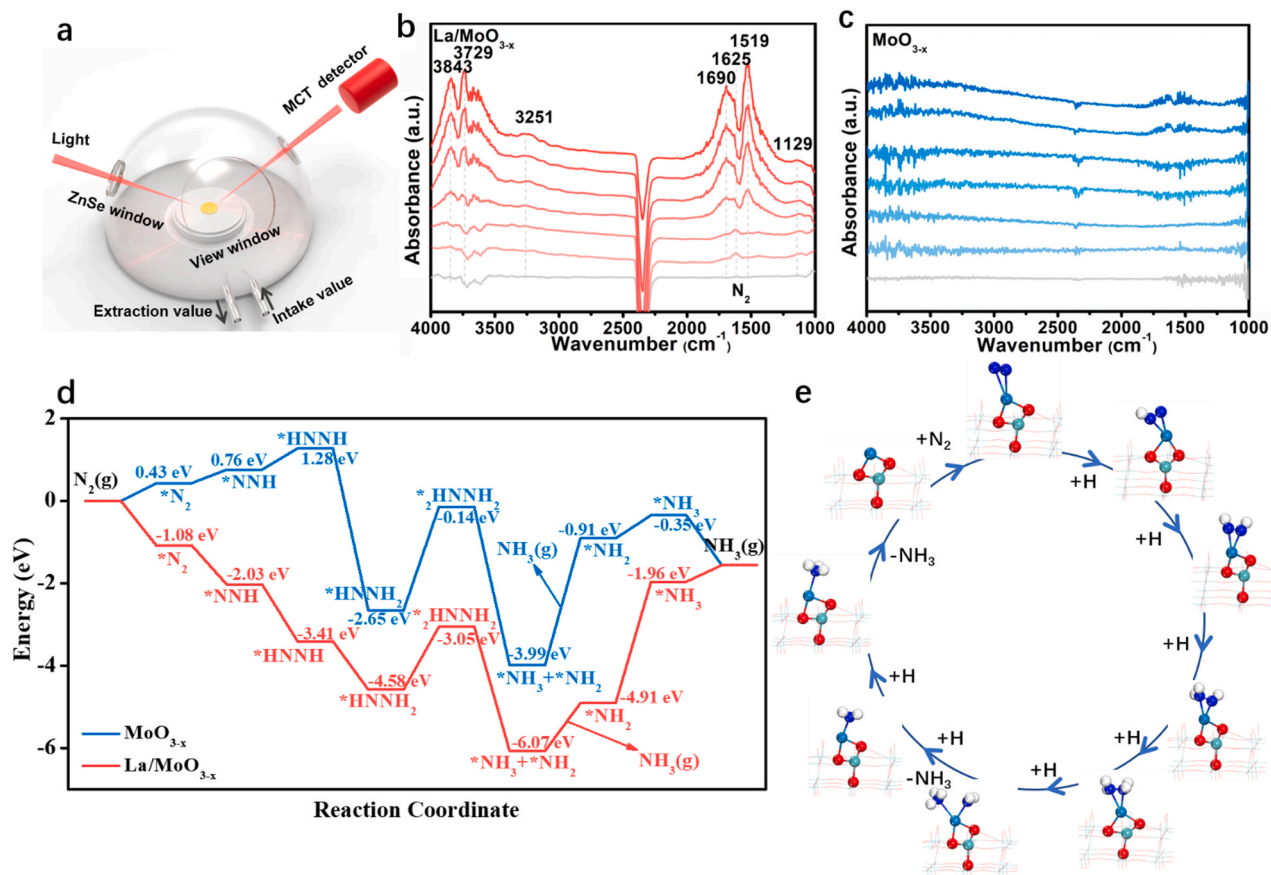


Fig. 4. (a) Diagram of the in-situ FT-IR setup. (b) In situ FT-IR spectra of N_2 fixation on La/MoO_{3-x} and (c) MoO_{3-x} . (d) Reaction energy diagram of nitrogen fixation photocatalyzed by La/MoO_{3-x} and MoO_{3-x} . (e) The diagram of reaction process on O_{2c} -La- O_{2c} site.

that hydrazine (H_2NNH_2) is the key intermediate in photocatalytic ammonia synthesis [35], and such species are detected by in situ FT-IR over the O_{2c} -La- O_{2c} site. However, that peak is not detected for MoO_{3-x} , suggesting that the hydrogenation process would be probably terminated at the H_2NNH_2 intermediate. The DFT results also demonstrate that the conversion of $*NHNH_2$ to H_2NNH_2 is an uphill pathway with 1.53 eV and 2.51 eV (La/MoO_{3-x} and MoO_{3-x} , respectively), the MoO_{3-x} surface inhibits this process. The remaining hydrogenation and ammonia desorption processes are consistent with the side-on pathway, and the overall reaction process and the free energy of intermediate are depicted in Fig. 4e and Fig. S17. Overall, the above experiments and calculations reveal that the anchored single La atom spontaneously promotes N_2 activation and dominates the photocatalytic nitrogen fixation.

4. Conclusions

We report a single La atom catalyst with specific coordination structure for photocatalytic N_2 fixation. The single La atom catalyst gives a strong N_2 activation ability and a large ammonia yield of $209.0 \mu mol h^{-1} g^{-1}$. According to HAADF-STEM and XAFS experiments, the specific coordination of single La atom is identified to be O_{2c} -La- O_{2c} . The chemisorption experiments and DFT calculations suggest that the single La atoms optimize the local/intrinsic electron properties, favor the transfer of electrons into the $\pi^* 2p$ antibonding orbital of the adsorbed N_2 , thus confirming the origin of impressive photocatalytic activity. This work offers a potential SACs for the photocatalytic ammonia synthesis, also puts forward a new rational coordination of single La atom applied in photocatalytic reaction.

CRediT authorship contribution statement

Yani Luo performed the experiments. Cancan Ling contributed to final revision and visualization. Yanbiao Shi contributed to the check of the experiments' data. Hao Li contributed to the writing modification. Guangming Zhan contributed to the assistance of theoretical analysis. Huayu Gu, Kai Wei and Furong Guo contributed to the revision of the manuscripts.

Declaration of Competing Interest

The authors declare that they have no known competing financial interests or personal relationships that could have appeared to influence the work reported in this paper.

Acknowledgments

This work was supported by the National Key Research and Development Program of China (2016YFA0203000); National Science Foundation of China (U20A20129, 21876058); and the Excellent Doctoral Dissertation Cultivation Grant from Central China Normal University (2017YBZZ018).

Conflict of interest

The authors declare no competing financial interest.

Appendix A. Supporting information

Supplementary data associated with this article can be found in the

online version at doi:10.1016/j.apcatb.2021.120766.

References

- [1] J.W. Erisman, M.A. Sutton, J. Galloway, Z. Klimont, W. Winiwarter, How a century of ammonia synthesis changed the world, *Nat. Geosci.* 1 (2008) 636–639.
- [2] I. Rafiqul, C. Weber, B. Lehmann, A. Voss, Energy efficiency improvements in ammonia production—perspectives and uncertainties, *Energy* 30 (2005) 2487–2504.
- [3] J.G. Chen, R.M. Crooks, L.C. Seefeldt, K.L. Bren, R.M. Bullock, M.Y. Darensbourg, P.L. Holland, B. Hoffman, M.J. Janik, A.K. Jones, M.G. Kanatzidis, P. King, K. M. Lancaster, S.V. Lymar, P. Pfromm, W.F. Schneider, R.R. Schrock, Beyond fossil fuel-driven nitrogen transformations, *Science* 360 (2018) 6391.
- [4] H. Liu, P. Wu, H. Li, Z. Chen, L. Wang, X. Zeng, Y. Zhu, Y. Jiang, X. Liao, B. S. Haynes, J. Ye, C. Stampfl, J. Huang, Unravelling the effects of layered supports on Ru nanoparticles for enhancing N₂ reduction in photocatalytic ammonia synthesis, *Appl. Catal. B-Environ.* 259 (2019), 118026.
- [5] Z.-K. Shen, M. Cheng, Y.-J. Yuan, L. Pei, J. Zhong, J. Guan, X. Li, Z.-J. Li, L. Bao, X. Zhang, Z.-T. Yu, Z. Zou, Identifying the role of interface chemical bonds in activating charge transfer for enhanced photocatalytic nitrogen fixation of Ni₂P-black phosphorus photocatalysts, *Appl. Catal. B-Environ.* 295 (2021), 120274.
- [6] R. Guan, D. Wang, Y. Zhang, C. Liu, W. Xu, J. Wang, Z. Zhao, M. Feng, Q. Shang, Z. Sun, Enhanced photocatalytic N₂ fixation via defective and fluoride modified TiO₂ surface, *Appl. Catal. B-Environ.* 282 (2020), 119580.
- [7] W. Qiu, N. Yang, D. Luo, J. Wang, L. Zheng, Y. Zhu, E.M. Akinoglu, Q. Huang, L. Shui, R. Wang, G. Zhou, X. Wang, Z. Chen, Precise synthesis of Fe–N₂ with N vacancies coordination for boosting electrochemical artificial N₂ fixation, *Appl. Catal. B-Environ.* 293 (2021), 120216.
- [8] K. Fujiwara, S.E. Pratsinis, Single Pd atoms on TiO₂ dominate photocatalytic NO_x removal, *Appl. Catal. B-Environ.* 226 (2018) 127–134.
- [9] A. Wang, J. Li, T. Zhang, Heterogeneous single-atom catalysis, *Nat. Rev. Chem.* 2 (2018) 65–81.
- [10] B. Wang, H. Cai, S. Shen, Single metal atom photocatalysis, *Small Methods* 3 (2019), 1800447.
- [11] Z. Li, S. Ji, Y. Liu, X. Cao, S. Tian, Y. Chen, Z. Niu, Y. Li, Well-defined materials for heterogeneous catalysis: from nanoparticles to isolated single-atom sites, *Chem. Rev.* 120 (2020) 623–682.
- [12] K. Liu, X. Zhao, G. Ren, T. Yang, Y. Ren, A.F. Lee, Y. Su, X. Pan, J. Zhang, Z. Chen, J. Yang, X. Liu, T. Zhou, W. Xi, J. Luo, C. Zeng, H. Matsumoto, W. Liu, Q. Jiang, K. Wilson, A. Wang, B. Qiao, W. Li, T. Zhang, Strong metal-support interaction promoted scalable production of thermally stable single-atom catalysts, *Nat. Commun.* 11 (2020) 1263.
- [13] P. Huang, W. Liu, Z. He, C. Xiao, T. Yao, Y. Zou, C. Wang, Z. Qi, W. Tong, B. Pan, S. Wei, Y. Xie, Single atom accelerates ammonia photosynthesis, *Sci. Chin. Chem.* 61 (2018) 1187–1196.
- [14] Y. Gu, B. Xi, W. Tian, H. Zhang, Q. Fu, S. Xiong, Boosting selective nitrogen reduction via geometric coordination engineering on single-tungsten-atom catalysts, *Adv. Mater.* 33 (2021), e2100429.
- [15] Y.Y. Jin, P.P. Hao, R. Jun, L. Zhong, Single atom catalysis: concept, method and application, *Prog. Chem.* 27 (2015) 1689.
- [16] S. Zhang, Y. Zhao, R. Shi, C. Zhou, G.I.N. Waterhouse, L.Z. Wu, C.H. Tung, T. Zhang, Efficient photocatalytic nitrogen fixation over Cu modified defective ZnAl-layered double hydroxide nanosheets, *Adv. Energy Mater.* 10 (2020), 1901973.
- [17] P. Chen, B. Lei, X. Dong, H. Wang, J. Sheng, W. Cui, J. Li, Y. Sun, Z. Wang, F. Dong, Rare-earth single-atom La–N charge-transfer bridge on carbon nitride for highly efficient and selective photocatalytic CO₂ reduction, *ACS Nano* 14 (2020) 15841–15852.
- [18] H. Li, C. Mao, H. Shang, Z. Yang, Z. Ai, L. Zhang, New opportunities for efficient N₂ fixation by nanosheet photocatalysts, *Nanoscale* 10 (2018) 15429–15435.
- [19] H. Cheng, X. Qian, Y. Kuwahara, K. Mori, H. Yamashita, A. Plasmonic, Molybdenum oxide hybrid with reversible tunability for visible-light-enhanced catalytic reactions, *Adv. Mater.* 27 (2015) 4616–4621.
- [20] H. Yin, Y. Kuwahara, K. Mori, H. Cheng, M. Wen, H. Yamashita, High-surface-area plasmonic MoO_{3-x}: rational synthesis and enhanced ammonia borane dehydrogenation activity, *J. Mater. Chem. A* 5 (2017) 8946–8953.
- [21] X.L. Ma, J.C. Liu, H. Xiao, J. Li, Surface single-cluster catalyst for N₂-to-NH₃ thermal conversion, *J. Am. Chem. Soc.* 140 (2018) 46–49.
- [22] S.J. Clark, M.D. Segall, C.J. Pickard, P.J. Hasnip, M.I. Probert, K. Refson, M. C. Payne, First principles methods using CASTEP, *Z. für Krist. -Cryst. Mater.* 220 (2005) 567–570.
- [23] E.R. McNellis, J. Meyer, K. Reuter, Azobenzene at coinage metal surfaces: role of dispersive van der Waals interactions, *Phys. Rev. B* 80 (2009), 205414.
- [24] J. Li, S. Chen, F. Quan, G. Zhan, F. Jia, Z. Ai, L. Zhang, Accelerated dinitrogen electroreduction to ammonia via interfacial polarization triggered by single-atom protrusions, *Chem* 6 (2020) 885–901.
- [25] Y. Zhao, Y. Zhao, R. Shi, B. Wang, G.I.N. Waterhouse, L.Z. Wu, C.H. Tung, T. Zhang, Tuning oxygen vacancies in ultrathin TiO₂ nanosheets to boost photocatalytic nitrogen fixation up to 700 nm, *Adv. Mater.* 31 (2019), 1806482.
- [26] J. Han, X. Ji, X. Ren, G. Cui, L. Li, F. Xie, H. Wang, B. Li, X. Sun, MoO₃ nanosheets for efficient electrocatalytic N₂ fixation to NH₃, *J. Mater. Chem. A* 6 (2018) 12974–12977.
- [27] M. Dieterle, G. Weinberg, G. Mestl, Raman spectroscopy of molybdenum oxides, *Phys. Chem. Chem. Phys.* 4 (2002) 812–821.
- [28] Z. Wan, M. Hu, B. Hu, T. Yan, K. Wang, X. Wang, Vacancy induced photocatalytic activity of La doped In(OH)₃ for CO₂ reduction with water vapor, *Catal. Sci. Technol.* 10 (2020) 2893–2904.
- [29] Y. Yang, L.C. Yin, Y. Gong, P. Niu, J.Q. Wang, L. Gu, X. Chen, G. Liu, L. Wang, H. M. Cheng, An unusual strong visible-light absorption band in red anatase TiO₂ photocatalyst induced by atomic hydrogen-occupied oxygen vacancies, *Adv. Mater.* 30 (2018), 1704479.
- [30] C. Mao, H. Cheng, H. Tian, H. Li, W. Xiao, H. Xu, J. Zhao, L. Zhang, Visible light driven selective oxidation of amines to imines with BiOCl: does oxygen vacancy concentration matter? *Appl. Catal. B-Environ.* 228 (2018) 87–96, 97–96.
- [31] J. Li, L. Cai, J. Shang, Y. Yu, L. Zhang, Giant enhancement of internal electric field boosting bulk charge separation for photocatalysis, *Adv. Mater.* 28 (2016) 4059–4064.
- [32] Y. Zhao, Y. Zhao, G.I.N. Waterhouse, L. Zheng, X. Cao, F. Teng, L.Z. Wu, C.H. Tung, D. O'Hare, T. Zhang, Layered-double-hydroxide nanosheets as efficient visible-light-driven photocatalysts for dinitrogen fixation, *Adv. Mater.* 29 (2017), 1703828.
- [33] T. Wu, X. Zhu, Z. Xing, S. Mou, C. Li, Y. Qiao, Q. Liu, Y. Luo, X. Shi, Y. Zhang, X. Sun, Greatly improving electrochemical N₂ reduction over TiO₂ nanoparticles by iron doping, *Angew. Chem. Int. Ed. Engl.* 58 (2019) 18449–18453.
- [34] L. Shi, Z. Li, L. Ju, A. Carrasco-Pena, N. Orlovskaya, H. Zhou, Y. Yang, Promoting nitrogen photofixation over a periodic WS₂@TiO₂ nanoporous film, *J. Mater. Chem. A* 8 (2020) 1059–1065.
- [35] J. Zhao, Z. Chen, Single Mo atom supported on defective boron nitride monolayer as an efficient electrocatalyst for nitrogen fixation: a computational study, *J. Am. Chem. Soc.* 139 (2017) 12480–12487.